Design a Bi-directional DC-DC Converter for Optimizing Energy Storage in Electric Vehicles (EVs)

1. Nakka Archana
EEE, GNITS
Shaikpet, Hyderabad, India
archanabhaskernakka124@gmail.com

2. G. Ramana Reddy
EEE, GNITS
Shaikpet, Hyderabad, India
grreddy72@gnits.ac.in

***ABSTRACT*—THE PRESENT WORK DESCRIBES THE IMPLEMENTATION AND CONTROL OF A HIGHLY EFFICIENT POWER CONVERSION ARCHITECTURE THAT IS DESIGNED SPECIFICALLY FOR ELECTRIC VEHICLES (EV), ALLOWING IT TO PERFORM BOTH MOTOR DRIVING AND ONBOARD BATTERY CHARGING FUNCTIONS. THE SYSTEM PRESENTED IN THIS STUDY EMPLOYS A GRID CONNECTED INTERLEAVED TOTEM POLE CONVERTER AS THE FRONT STAGE BIDIRECTIONAL AC/DC INTERFACE. IT PROVIDES PFC AND CAN FUNCTION AS A THREE PHASE INVERTER BY TIME MULTIPLEXING OF A FULL BRIDGE. THE ADVANTAGES OF THIS SYSTEM INCLUDE: LOWER LOSS DUE TO LESS CONDUCTING PATHS; HIGHER EFFICIENCY; LESS RIPPLE WITHIN THE INPUT CURRENT WAVEFORM; AND CLOSE TO NEAR-UNITY POWER FACTOR OPERATION. ADDITIONALLY, THE SYSTEM CAN ALSO BE CONTROLLED TO OPERATE AS A MOTOR CONTROLLER. THE REAR STAGE UTILIZES A DAB DC–DC CONVERTER INTEGRATED WITH A HIGH-FREQUENCY TRANSFORMER FOR ELECTRICAL ISOLATION; BI-DIRECTIONAL POWER TRANSFER; AND HIGH POWER DENSITY SUITABLE FOR FAST CHARGE AND DRIVE. AN ANN-BASED CONTROL METHOD WILL BE USED FOR ENHANCING THE OVERALL DYNAMIC AS WELL AS STEADY-STATE BEHAVIOR ACROSS ALL OF THE VARIOUS OPERATING MODES. CONVENTIONAL DOUBLE CLOSED LOOP CONTROL METHODS WILL ALSO BE EMPLOYED. A SMALL-SIGNAL REPRESENTATION OF EACH OF THE TWO CONVERTER STAGES IS DEVELOPED IN ORDER TO PROPERLY SELECT CONTROLLERS AND DETERMINE HOW THEY WOULD INTERACT. SIMULATIONS WERE PERFORMED THROUGH MATLAB/SIMULINK SIMULATIONS TO VERIFY THE EFFECTIVENESS OF THE DEVELOPED SYSTEM. THESE SIMULATIONS DEMONSTRATED AN ENHANCEMENT IN OVERALL EFFICIENCY, REDUCTION IN TOTAL HARMONIC DISTORTION, IMPROVEMENT IN TRANSIENT RESPONSE, AND STABLE OPERATION OVER A WIDE RANGE OF CHARGE/DISCHARGE STATES.**

***Keywords* - Electric vehicles (EVs), on-board charger, interleaved totem-pole converter, dual active bridge (DAB) converter, bidirectional power flow, power factor correction (PFC), artificial neural network (ANN), model predictive control (MPC), permanent magnet synchronous motor (PMSM), regenerative braking, grid-to-vehicle (G2V), vehicleto-grid (V2G).**

I. INTRODUCTION

The world's need for transportation is likely going to grow faster than ever before over the next few decades because of the rapidly growing population around the globe, increasing incomes, and easier access to all types of transportation systems [1], [2]. As stated by the International Energy Agency (IEA), the world's need for transportation will be at least double what it currently is by 2070, creating large increases in both energy usage and greenhouse gas emissions [3]. Because of this need, Electric Vehicles (EVs) have become a very attractive option to achieve efficient and sustainable forms of transportation. Presently, each component within an EV architecture has separate dedicated systems. For example, one system would drive the vehicle while another would charge the onboard batteries. This creates larger, heavier, and more expensive systems [4]. To help mitigate some of the issues associated with present-day EV architectures, much interest is being directed toward integrating the onboard charging system with the driving system. The integration of the two can result in a higher power density, less redundant hardware, and greater overall efficiencies. One major component within the onboard charging system includes an AC/DC converter. It interfaces the direct-current (DC) battery toward the AC grid. A major requirement for use on the AC grid, according to grid standards such as IEC 61000-3-2, is to have high power factors and low total harmonic distortions (THDs). Therefore, Power Factor Correction (PFC) circuits are commonly used in onboard charging configurations [5]-[7]. High-power-factor PFC circuits typically employ a boost-type configuration. Unfortunately, using a diode bridge rectifier results in loss conduction, thereby reducing the overall system efficiency. Several alternative configurations have been developed to improve upon existing PFC circuitry. Some of these alternatives include SEPIC/CUK-type PFC circuits, Buck-Buck-type PFC circuits, and Boost-type PFC circuits [8]–[11]. Among those alternatives, the Totem-Pole PFC Converter has garnered particular interest for its high efficiency, lower conduction losses, and increased power density [12]. However, the switching losses and conduction losses inherent within the Totem Pole PFC Configuration necessitate the development of optimized design and control methods to improve overall performance and efficiency in practical applications [13], [14]. Bidirectional non-isolated DC–DC converters can be utilized for energy transfer from battery side to the dc link (and vice versa) in an EV charging system. These converters are generally classified into two categories: isolated and non-isolated topologies. Advantages of the non-isolated converter include lower cost, simpler structure, and higher efficiencies compared with other types. However, there are some disadvantageous characteristics associated with this type including lower voltage gain and lack of galvanic isolation. Due to their low cost and ability to fit into space-constrained applications with little weight concern, non-isolated converters are well suited for many applications [15]. Isolated converters utilize high-frequency transformers to provide electrical isolation and flexibility in converting voltages. Although isolated converters offer better protection and flexibility than non-isolated converters, they are also larger and more costly. Therefore, isolated converters may be more suited for applications where electrical safety and isolation are important. Many different bi-directional non-isolated DC–DC converter configurations have been extensively investigated.

Representative examples of these configurations include Buck/Buck, Buck-Boost, Cuk, Sepic Interleaved Quasi-Z-Source H-Bridge Cascaded Structures, etc. [17], [18]. Despite their advantages, many of these configurations experience problems including limited voltage gain, reduced power density, and compromises in performance based on operational conditions, which can hinder their effectiveness in practical applications. Bidirectional converters that operate independently provide high voltage ratios and superior safety features via isolation transformers, making them highly attractive for high-power EV applications [19]-[21]. The DAB converter is one of the most widely studied among all single phase isolated topologies due to the fact that it enables bi-directional power transfer in high efficiency manner at high frequencies; and therefore can be used for various purposes [22]-[23], while advanced semiconductor materials such as SiC- and GaN-based devices are capable of decreasing the loss generated by the switching operation of the devices and consequently increase the global efficiency of the system [24]-[25]. While great advances have been made in converter configurations, the control strategies used for EV charging systems are still one of the most important aspects. Electric vehicles (EVs) utilize permanent magnet synchronous motors (PMSMs) as traction systems, primarily because they offer higher efficiency, higher power density, and reliable operation [26]-[27]. Most PMSM drives traditionally use vector-based control (VC) [28] or direct torque-based control [29] to control the drive systems. Vector control offers excellent steady-state performance; however, VC relies upon proportional-integral (PI) controllers. PI controllers are very difficult to tune and produce many intermediate variables, which can complicate the control process and lead to suboptimal performance in the drive systems. In comparison, DTC produces faster transient responses than VC but generates significant amounts of torque ripple and high-frequency noise that degrade system performance. Thus, researchers have explored a number of new advanced control strategies such as sensorless position control [30], SMC technique [31], fault-adaptive control [32], and prediction-based control [33] to address these disadvantages. Predictive control has attracted considerable research interest recently due to the tremendous growth in digital signal processing (DSP) technology and enhanced computational capabilities of today's microprocessors. Deadbeat-based predictive control (DPC) [34], Hysterisis Predictive Control [35], Trajectory Predictive Control [36] and Model Methodologies can be broadly categorized into four classes: MPC strategy. The merits of each method include different characteristics regarding transient response speeds and prediction errors. Both DPC and MPC are used for PMSM drive systems among these methods. A deadbeat predictive control provides both accurate predictions and fast transients by defining the input actions according to the discrete-time model of the controlled system. MPC defines the control actions which will provide an optimal response based on predictions made of future states of the plant over some fixed time period. In addition, MPC can also predict multiple control variables. Also, MPC is effective at managing nonlinearities and time varying behaviors related to PMSMs. Therefore, MPC is suitable for PMSM drive systems that exhibit considerable nonlinearity and coupling effects. Consequently, predictive control has received extensive attention for increasing the dynamic performance, stability and reliability of EV motor drive systems under various operating conditions [37]. Due to their ease of implementation, proportional-integral (PI) controllers are commonly employed in control systems. However, PI controllers typically perform poorly under non-linear and dynamic operating conditions, resulting in lower system stability and power quality. Therefore, artificial neural network (ANN)-based control schemes have gained increasing attention within power electronics applications. ANN-based control methodologies have successfully been implemented for fault diagnosis, voltage sag classification, and short-term forecasting as well as having less computational complexity [38]-[41]. ANN learns the behavior of the system based on past data to generate quicker and more precise control actions than traditional methodologies. A hybrid PI/ANN control strategy is introduced in this study for an integrated EV charging system and motor drive. The PI controller ensures steady-state regulation, while the ANN enhances the dynamic performance by compensating for non-linearity and uncertainty [42]. The proposed system employs an interleaved totem-pole PFC converter for the front-end stage together with a dual active bridge (DAB) converter within the back-end stage, resulting in enhanced efficiency, diminished harmonic distortion, and superior power quality. Simulation results using MATLAB/Simulink demonstrate that the proposed system operates stably and reliably under several EV charging/driver scenarios.

The proposed integrated motor drive and onboard charging architecture provides the following main contributions:

1 A New Method for Converting AC electrical energy into DC power With Ability to Drive Electric Motors and Charge Batteries Will Be Introduced. This will reduce the number of components needed, the physical space required, and thus the total cost.

2. The front stage PFC/inverter is able to function as a single unit by multiplexing its switching action between PFC and inverter modes. It has achieved very high efficiencies at all loads, minimal conduction losses, extremely low input current ripple, nearly unity power factor, and enables motor control capabilities.

3. The DAB Converter achieves galvanic isolation and provides high voltage gain, bidirectional DC/DC power flow across diverse operating conditions while maintaining safe and reliably through the use of a high frequency transformer.

4. A hybrid control strategy utilizing both traditional PI–ANN based control approach control was implemented to circumvent the inherent shortcomings of each individual control methodology. The combined methodologies improve upon the systems' steady state stability and dynamic responses, and greatly minimize the potential for excessive power variations due to non-linear and changing operating conditions.

5. The ANN controller generates optimized pulse width modulation (PWM) signal duty cycles in real-time. The resulting reduction in computational requirements allows for greater precision in the tracking of desired outputs, better overall power quality, and increased system performance when compared to traditionally employed control strategies.

6. SIMULATIONS WERE RUN IN MATLAB/SIMULINK AND DEMONSTRATED IMPROVEMENTS IN EFFICIENCY, REDUCTIONS IN HARMONIC DISTORTION, FASTER TRANSIENT PERFORMANCE,

AND CONSISTENT OPERATION DURING BOTH CHARGING AND DRIVING OPERATIONS

II. SYSTEM ARCHITECTURE AND OPERATIONAL CHARACTERISTICS

A. System Architecture and Operational Modes

The configuration presented in this article includes two primary sections as seen in Figure 1. The first or "front" section uses a three phase, fully controlled AC-DC bridge with bi-directional capability, performing both rectification and inversion. Using one unit versus using separate units for rectification and inversion results in fewer semiconductor components needed, therefore lower costs associated with the system and greater power density.

In section two there is Dual Active Bridge (DAB)-based bidirectional DC–DC converter, Which Allowing The Bi-Directional Energy Transfer And Separates Grid Side From Battery Side When It Being Charged. During the charging cycle relay K1 will be closed and relay K2 will be opened; an external input inductor can then be used. The front section of the converter acts as a bridgeless interleaved totem-pole PFC topology, reducing the current-induced stress on each switching device and increasing efficiency through synchronous rectification. The rear-section DAB converter is operating under forward power flow conditions to ensure soft-switching capabilities exist across a wide load spectrum and allow the battery to be constantly charged at either voltage or current levels (CV/CC). When the vehicle is running relay K1 will be open and relay K2 will be closed. With this setup the front section of the converter acts as an inverter controlling motor speed whereas the rear-stage DAB converter functions under reverse power flow by transferring energy from battery back to the inverter to provide power to operate the motor. An ANN/MPC control strategy was utilized for motor speed control in the driving cycle to produce rapid dynamic responses and better track performance. Additionally, the use of ANN-based control for the interleaved totem pole AC/DC converter enhanced power quality reduced total harmonic distortion and improved overall conversion efficiency. Therefore, the multi-control strategy allows for smooth transitions between charges and drive cycles and produces a highly efficient, reliable and stable system.

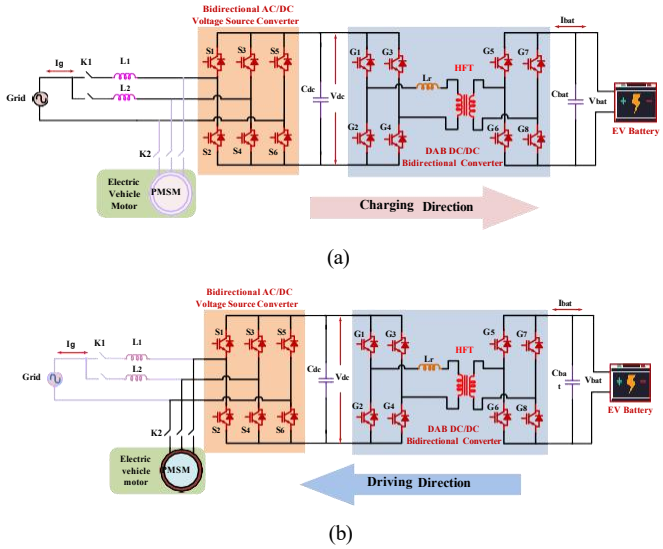

Fig. 1 (a) Charging mode, (b) Driving mode

B. Evaluation of AC/DC converters with bidirectional operation

Figure 2 shows the low conduction losses and high efficiency power conversion made possible by the interleaved totem-pole voltage-source converter (VSC) topology, which operates as a bidirectional alternating-current to direct-current converter for EV applications. The topology consists of two interleaved inductors L_1 and L_2, a set of six switches S_1–S_6, and a DC-link capacitor C_{dc} . The interleaving technique ensures ripple cancellation and improved current sharing, while the totem-pole structure eliminates the diode bridge.

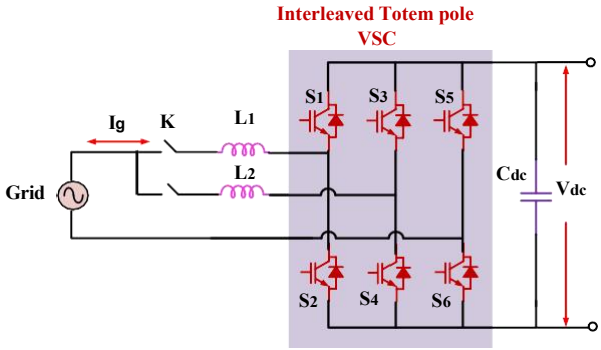

Fig. 2 Topology of Interleaved Bridgeless Totem-Pole PFC Topology

It is possible in order to study this converter with respect to relation to the switching conditions associated with the upper and lower devices, while its operation is dependent upon the polarity of the grid voltage polarity V_g. The instantaneous total current flowing through the inductor is known as the defined as the input current:

$$i_g(t) = i_{L1}(t) + i_{L2}(t) \quad (1)$$

While S_2, S_4 , and S_6 provide synchronous rectification channels, switches S_1 , S_3 , and S_5 function as high-frequency switching devices during throughout the positive half-cycle of the grid voltage vg>0.

This operation for each interleaved phase can be explained as follows:

To store energy, an appropriate inductor L_1 becomes connected to the grid and becomes active whenever the active switch (S_1) is switched activated. As a result, the inductive voltage becomes

$$v_{L1}(t) = v_g(t) \quad (2)$$

$$L_1 \frac{di_{L1}(t)}{dt} = v_g(t) \quad (3)$$

When the switch is deactivated, its stored energy is delivered to the connected DC-link capacitor through the complementary switch path, while the inductor voltage becomes

$$v_{L1}(t) = v_g(t) - V_{dc}(t) \quad (4)$$

$$L_1 \frac{di_{L1}(t)}{dt} = v_g(t) - V_{dc}(t) \quad (5)$$

Similarly, for the second phase:

$$L_2 \frac{di_{L2}(t)}{dt} = v_g(t) \text{ (ON state)} \quad (6)$$

$$L_2 \frac{di_{L2}(t)}{dt} = v_g(t) - V_{dc}(t) \text{ (OFF state)} \quad (7)$$

The two inductors operate with a phase shift (typically 180∘), which results in ripple cancellation. The effective ripple current is reduced as

$$\Delta i_g \approx \frac{\Delta i_L}{2} \quad (8)$$

Throughout the negative half-cycle vg<0, the operating roles of the switches become reversed. The bottom switches S2, S4, S6 operate at high frequency, while the upper switches provide the current path. However, the fundamental operation remains identical, and the same inductor equations apply:

$$L\frac{di_L}{dt} = v_g - v_{conv} \quad (9)$$

Integrating all of the inductors within a single switching cycle according to the volt-second balancing principle:

$$d \cdot v_g + (1-d)(v_g - V_{dc}) = 0 \quad (10)$$

which gives the DC-link voltage relationship:

$$V_{dc} = \frac{v_g}{1-d} \quad (11)$$

The DC-link capacitor maintains the output voltage, and its dynamics are given by:

$$C_{dC}\frac{dV_{dC}(t)}{dt} = i_{L1}(t) + i_{L2}(t) - i_{load}(t) \quad (12)$$

Thus,

$$C_{dC}\frac{dV_{dC}(t)}{dt} = i_g(t) - i_{load}(t) \quad (13)$$

The interleaved totem pole configuration has been developed to provide improved current ripple reduction in the system, improved efficiency through elimination of the conducting losses that occur when a diode is active, and distribution of thermal stress across each switch to allow for the operation at high performance levels as a boost-type AC/DC converter. It will therefore offer high-quality power, reduced harmonic distortion, and increased efficiency. Overall, it could thus be viewed as an effective solution for use in an Electric Vehicle (EV) on-board charging system.

C. Bidirectional AC/DC converter control strategy

The controller for the interleaved totem pole converter consists of multiple functional elements that are synchronized with each other. To satisfy both enhanced power factor performance and low harmonic distortion specifications while simultaneously maintaining a steady DC-link voltage at all times across variable operation operating conditions, as shown in Fig. 3, these functions include a dc link voltage regulator; an ANN based modulator; reference current generator; interleaved current controller; ZCD circuitry; and a logic switching network.

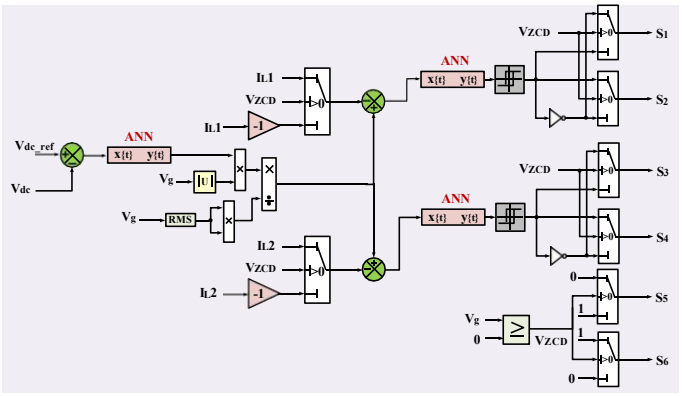

Fig.3 ANN-Based Control Scheme of the Interleaved Totem-Pole AC/DC Converter

a. DC-Link Voltage Error Signal Generation

Managing the DC-link voltage becomes the first step in the control procedure. The resultant inaccuracy is given by comparing the desired voltage V_{dc}^{ref} against the actual DC-link output voltage $V_{dC}(t)$.

$$e_v(t) = V_{dc}^{ref} - V_{dC}(t) \quad (14)$$

b. ANN-Based Voltage Controller

The voltage error and its derivative are processed by an ANN-based controller, which replaces the conventional PI controller. The ANN generates the reference current magnitude required for regulating the DC-link voltage:

$$I_{ref} = ANN_v(e_v(t), \dot{e}_v(t)) \quad (15)$$

The ANN predicts the nonlinear relationship between the voltage error in relation to the needed input current. This provides a better response time and greater resistance to system nonlinearities and disturbances.

c. Grid Synchronization and Reference Current Generation

In order for unity power-factor operation to be achieved, the input current must follow the grid-voltage waveform. Thus, the measured grid-voltage signal $v_g(t)$, from the Control Structure is processed by an Absolute Value and RMS Block so that it may be normalized.

$$V_{g,rms} = \sqrt{\frac{1}{T}\int_0^T v_g^2(t)dt} \quad (16)$$

The normalized grid signal is given by

$$v_{norm}(t) = \frac{v_g(t)}{V_{g,rms}} \quad (17)$$

Thus, the reference current is generated as

$$i_g^*(t) = I_{ref} \cdot v_{norm}(t) \quad (18)$$

This maintains sinusoidality and phase alignment of the input current with the grid voltage.

d. Interleaved Current Splitting

In the interleaved converter configuration, the total input current is distributed over two inductors L_1 and L_2 which increases the capacity to handle current and decreases ripple. can be represented as:

$$i_g(t) = i_{L1}(t) + i_{L2}(t) \quad (19)$$

Each inductor current is controlled independently, allowing balanced current sharing and improved efficiency.

5. Current Error Generation (Per Phase)

In each interleaved phase, the measured phase inductor current becomes compared against the reference current to produce an error signal. For Phase 1 and Phase 2, the error signals for the currents are defined as:

$$e_{i1}(t) = i_g^*(t) - i_{L1}(t) \quad (20)$$

$$e_{i2}(t) = i_g^*(t) - i_{L2}(t) \quad (21)$$

Derivatives of these errors are used to provide improved transient performance. These signals indicate how far off each phase's current is from its desired output.

e. ANN-Based Current Controllers

ANN-based current controllers process the current error signals and their derivatives for each phase and generate the necessary duty cycle commands:

$$d_1 = ANN_1(e_{i1}, \dot{e}_{i1}) \quad (22)$$

$$d_2 = ANN_2(e_{i2}, \dot{e}_{i2}) \quad (23)$$

The generated duty cycle commands define the switching actions that take place at each of the individual converter legs. In comparison with traditional control systems, ANN provides a significantly quicker response time and greater ability to compensate for non-linear responses.

f. Zero-Crossing Detection (ZCD)

ZCD (Zero Crossing Detection) indicates the correct direction of the Grid Voltage. This is critical to allow for appropriate operation of the Totem Pole Converter.

$$v_{ZCD} = \begin{cases} 1, & v_g(t) \geq 0 \\ 0, & v_g(t) < 0 \end{cases} \quad (24)$$

This signal ensures that the correct switching devices are activated during positive and negative phases of the grid voltage.

g. Switching Logic Operation

The switching logic uses the ZCD signal and duty cycles to generate appropriate gating signals for the switches.

(a) Upper Switches S_1– S_2: During the positive half-cycle (VZCD=1), switches S_1 and S_3 operate as active switches, while S2 and S4 act as complementary switches:

$$S_2 = S_1 \quad (25)$$

$$S_4 = S_3 \quad (26)$$

During the negative half-cycle (VZCD=0), the roles are reversed:

$$S_1 = S_2 \quad (27)$$

$$S_3 = S_4 \quad (28)$$

(b) Grid-Side Switches S_5 and S_5: The grid-side switches are directly controlled by the ZCD signal:

$$S_5 = V_{ZCD} \quad (29)$$

$$S_6 = \bar{V}_{ZCD} \quad (30)$$

Consequently, S_5 is active throughout the positive half-cycle, whereas S_6 operates during the negative half-cycle.

h. PWM Signal Generation

The duty cycles generated by the ANN controllers are converted into switching signals using PWM. The switching condition is given by

$$S(t) = \begin{cases} 1, & d(t) > V_{carrier}(t) \\ 0, & d(t) \leq V_{carrier}(t) \end{cases} \quad (31)$$

This process ensures proper modulation of the converter switches.

III. MODELLING AND DESIGNING OF LITHIUM-ION EV BATTERY

A. Electrochemical Fundamentals

Rechargeable Lithium-Ion Batteries work using reversible lithium ion insertion (into the cathode) and extraction (from the cathode) by way of reversible chemical oxidation/reduction in which Lithium-ions move between the Cathodic Transition Metal Oxide electrode and the Graphite Anode. This allows for good efficiency with regard to Energy Storage and Release. Since this process does not involve the formation of Lithium metal at either Electrode it is safer than other rechargeable battery technologies and has better Cycle Life. In order for an electrochemical cell to function correctly, an electrolyte must be present to facilitate the movement of lithium ions between the cathode and anode while simultaneously preventing the transmission of electrons. A complete electrochemical reaction in a Li-ion cell would seem like this during both charging and discharging [43][44]:

$$Li_xC_6 + Li_{1-x}M_yO_z \rightleftharpoons C_6 + LiM_yO_z \quad (32)$$

where:

- Li_xC_6 represents the lithiated graphite anode,
- $Li_{1-x}M_yO_z$ represents the partially lithiated cathode material,
- M denotes the transition metal (such as Co, Fe, or Mn),
- x represents the degree of lithium intercalation.

Common types of lithium compounds used as cathodes include ($L_iF_ePO_4$), ($L_iMn_2O_4$), and ($L_iC_oO_2$).

a. Anode Reaction

At the graphite anode, lithium ions are stored within the layered carbon structure during charging and released during discharging. The electrochemical reaction at the anode during discharge is given by:

$$Li_xC_6 \longrightarrow C_6 + xLi^+ + xe^- \quad (33)$$

The process of lithium ions intercalating into the graphite lattice happens in the opposite way during charging.

b. Cathode Reaction

At the cathode, lithium ions are inserted into the transition metal oxide structure during discharge. The corresponding reaction is expressed as:

$$Li_{1-x}M_yO_z + xLi^+ + xe^- \longrightarrow LiM_yO_z \quad (34)$$

During charging, lithium ions are released from the cathode material, while the reaction reverses.

B. Modeling Batteries and Estimating Their State of Charge

The application of lithium-ion (Li-ion) batteries in electric vehicles (EVs) has been increasing rapidly because they have higher energy densities than most other types of batteries, longer lifetimes, and higher efficiencies. To enable engineers to be able to evaluate system behavior and design controls for EVs, a good battery model is needed. This is true especially if the goal of the engineer is to understand how well the battery will perform at different times while it is being charged or discharged. Because models need to be both accurate and computationally efficient, the equivalent electrical circuit model (ECM) is one of the most popular ways to model Li-ion batteries. The ECM is a representation of the battery that includes an open-circuit voltage source Voc(SOC), a series resistance R_s together with a parallel RC network which represents the polarization that occurs as part of electrochemical reactions.

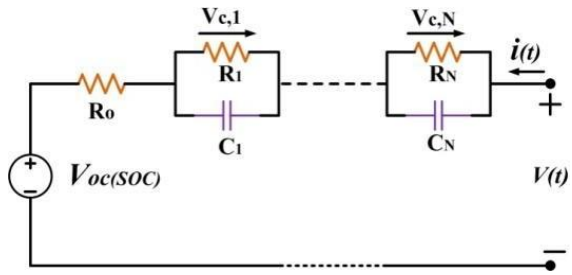

Fig. 4. Equivalent circuit diagram of lithium-ion EV battery

The voltage at the battery's terminals may be represented using the analogous circuit as

$$V(t) = V_{oc}(SOC) - I(t)R_s - V_{RC}(t) \quad (35)$$

where:

The voltage at the terminals is denoted as $V(t)$. The no-load voltage measured as dependent on SOC is denoted as $V_{oc}(SOC)$.The current through the battery, denoted as $I(t)$, is positive when discharged and negative when charged.The internal resistance is denoted as R_s.The RC polarization network voltage is denoted by $V_{RC}(t)$.

A first-order differential equation controls the polarization voltage's dynamic behavior:

$$\frac{dV_{RC}(t)}{dt} = -\frac{1}{R_pC_p}V_{RC}(t) + \frac{1}{C_p}I(t) \quad (36)$$

in which the parameters R_p and C_p denote the corresponding polarization resistive and capacitive components, respectively. This RC network captures transient voltage response due to electrochemical processes such as charge transfer and diffusion.

C. Estimation of the State of Charge (SOC)

Many battery monitoring systems (BMS) rely on state-of-charge (SOC), a crucial metric which represents the percentage of the battery's available energy remaining after depleting its maximum energy storage capacity. SOC's determination is generally accomplished by application of the coulomb-counting technique. This involves integration of the current being applied to the battery over time as follows:

$$SOC(t) = SOC(0) - \frac{1}{Q_{nom}}\int_0^t I(\tau)\,d\tau \quad (37)$$

where:

The initial state of charge, denoted as $SOC(0)$, the nominal battery capacity, denoted as Q_{nom} , and the instantaneous current, denoted as $I(\tau)$, are all variables.

For practical implementation, the discrete-time form is given by:

$$SOC(k+1) = SOC(k) - \frac{T_s}{Q_{nom}}I(k) \quad (38)$$

where Ts is the sampling time.

D. Open-Circuit Voltage (OCV–SOC Relationship)

Although experimental testing may identify the open-circuit terminal voltage, it is generally nonlinearly dependent on SOC. Approximate models of this relationship have been developed and are typically represented via polynomials or lookup tables as shown below:

$$V_{oc}(SOC) = a_0 + a_1 SOC + a_2 SOC^2 + \ldots\ldots + a_n SOC^m \quad (39)$$

A very accurate representation of the open circuit voltage is necessary for proper voltage predictions, and also for accurate battery-state estimations.

IV. CONTROL STRATEGY AND OPERATION OF ANN-BASED ON A DUAL ACTIVE BRIDGE CONVERTER

The proposed electric vehicle charging system employs the DAB converter, which functions as an electrically isolated bidirectional DC–DC converter. A High-Frequency Transformer (HFT) with leakage inductance L_r as illustrated in Fig. 5 connects the two full-bridge converters that comprise this module. The Primary Full-Bridge is connected to the dc-link bus voltage, V_{dc}, whereas the Secondary full-bridge converter has connection to the Battery Voltage, V_{bat}. This allows bi-directional power transfer, provides galvanic isolation, and also allows for high power density. The DAB is operated using Phase-Shift Modulation (PSM). PSM controls Power Transfer from the primary bridge side to the secondary bridge side through varying the phase-shift angle δ between the control functions of the Two Bridges. The waveforms created at both ends of the DAB are therefore Square-Wave Signals:

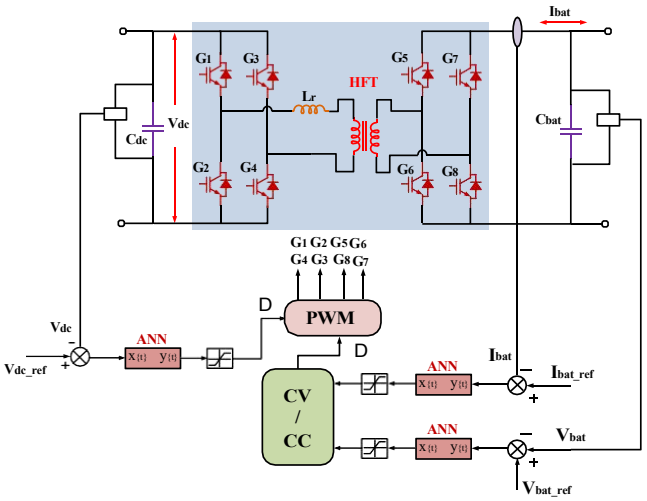

Fig.5 ANN-Based Control Strategy for Dual Active Bridge (DAB) Converter

$$v_1(t) = V_{dc} \cdot \text{sgn}(\sin(\omega t)) \quad (40)$$

$$v_2(t) = V_{bat} \cdot \text{sgn}(\sin(\omega t + \delta)) \quad (41)$$

The potential difference through the transformer leakage inductance produces the current:

$$L_r \frac{di_L(t)}{dt} = v_1(t) - nv_2(t) \quad (42)$$

Here n is the turns ratio of the transformer rotations. The corresponding DAB converter's average power transmission is provided by:

$$P = \frac{nV_{dlc}V_{bat}}{\omega L_r} . \delta \quad (43)$$

which indicates that the amount of transmitted power remains proportional to the phase-shift angle δ.

To regulate the battery charging process, constant-voltage /constant current (CV/CC) control strategy is adopted. The battery voltage and current are evaluated against their corresponding reference signals for generating control errors:

$$e_v(t) = V_{bat}^{ref} - V_{bat}(t) \quad (44)$$

$$e_i(t) = I_{bat}^{ref} - I_{bat}(t) \quad (45)$$

In the proposed method, artificial neural network (ANN) controllers are utilized to process these error signals. The ANN replaces conventional PI controllers and generates the appropriate control variable, namely the phase shift angle:

$$\delta = ANN(e, \dot{e}) \quad (46)$$

This approach enables faster dynamic response and improved handling of system nonlinearities.

The converter's operation is controlled by the CV/CC module. Starting with Constant Current Mode, the batteries are charged. Manage the current going into or out of the battery by adjusting this current. When the battery voltage reaches its maximum level, the CV mode takes over, as long as the battery voltage remains above that point the CV mode continues to regulate the output voltage. The delta produced by generating phase shift is inputted into the PWM module. The switching signals for switches G1–G8 are produced by the PWM modules. The phase difference created between the primary-side and secondary-side switch signals determines both the amount and direction of energy transfer. Power is moved from the direct current connection to the battery when δ is greater than 0, as in a charge cycle, and the inverse is true when δ is less than 0, as in a discharge cycle. Finally, under normal operating conditions the DAB converters may operate with zero voltage switching (zvs). zvs reduces switching losses resulting in greater efficiency. A necessary requirement for zvs is there must be enough current to produce a magnetic field within the leakage inductances of the transformer at each switch transition. Achieving accurate regulation of the battery voltage and current, enabling bidirectional power flow, and assuring efficient and dependable operation are all goals of the developed ANN-based control strategy for regulating the DAB converter. The inclusion of an ANN improves both dynamic response and reliability of the system, thus improving suitability for high performance electric vehicle (EV) charger application

V. DRIVING MODE CONTROL STRATEGY

A. Driving Mode of Voltage Source Inverter (VSI)

The proposed system in Drive Mode works in the same way as a Voltage Source Inverter (VSI); it supplies electric vehicle (EV) battery power to a PMSM drive motor using a Dual Active Bridge (DAB) converter, illustrated in Fig 6. The energy storage unit consists of the electric vehicle battery pack. The DAB converter performs as a bidirectional dc–dc converter to transfer and regulate power at the dc link side and provide galvanic insulation and bi-directional power flow capability. Following dc link regulation at V_{dc} the regulated dc link supply will be sent to the three phase VSI. That VSI will then convert the regulated dc power to controlled ac power for operating the PMSM.

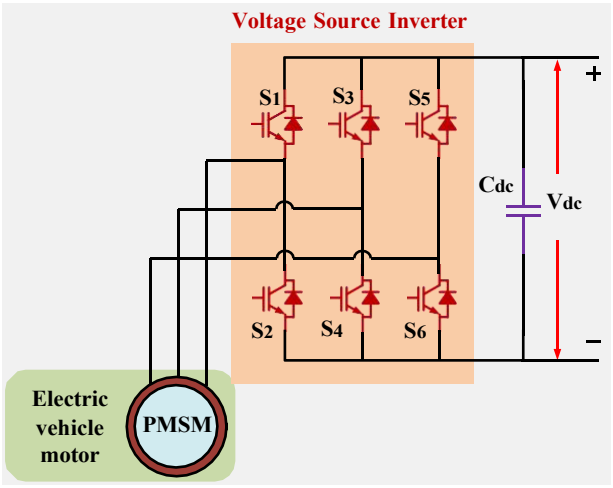

Fig.6 Electric Vehicle Drive System Using VSI-Fed PMSM

In relation to the DC-link midpoint, the phase voltages are provided by

$$v_a = \frac{V_{dlc}}{2}(S_1 - S_2) \quad (47)$$

$$v_b = \frac{V_{dlc}}{2}(S_3 - S_4) \quad (48)$$

$$v_c = \frac{V_{dlc}}{2}(S_5 - S_6) \quad (49)$$

where Si∈{0,1} denotes the switching state of each device. The corresponding line-to-line voltages are expressed as

$$v_{ab} = v_a - v_b \quad (50)$$

$$v_{bc} = v_b - v_c \quad (51)$$

$$v_{ac} = v_c - v_a \quad (52)$$

The PMSM will be subjected to these voltages in order to generate the required stator currents. The following is an explanation of the PMSM's dynamic behavior in terms of the Synchronous dq-Reference Frame:

$$v_d = R_s i_d + L_d \frac{di_d}{dt} - \omega_e L_q i_q \quad (53)$$

$$v_q = R_s i_q + L_q \frac{di_q}{dt} - \omega_e L_d i_d + \omega_e \lambda_f \quad (54)$$

The stator resistance, the inductances along the d- and q-axes, the electrical angular speed, and the permanent magnet flux linkage are all represented by the variables Rs, L_d, L_q, and λ_f, respectively.

The PMSM's electromagnetic torque is expressed as

$$T_e = \frac{3}{2} p(\lambda_f i_q + (L_d - L_q) i_d i_q) \quad (55)$$

In this case, "p" stands for the total number of pole pairs. It is common practice to achieve maximum torque per ampere (MTPA) in many electric vehicle applications by setting (id=0) (d-axis current). This means that the q-axis current has direct control over the electromagnetic torque.

Pulse Width Modulation (PWM) involves comparing the Reference Voltages with a High-Frequency Carrier Signal in order to create the PWM Inverter Switching Signals:

$$S(t) = \begin{cases} 1, & v_{ref}(t) > V_{carrier}(t) \\ 0, & v_{ref}(t) \le V_{carrier}(t) \end{cases} \quad (56)$$

This modulation ensures the generation of sinusoidal output voltages with controlled amplitude and frequency. During driving mode, the energy flow path is

$$Battery \rightarrow DAB\ Converter \rightarrow DC - Link \rightarrow VSI \rightarrow PMSM$$

The DAB converter controls dc-link voltage while controlling motor operation through VSI control (voltage, current & frequency). Therefore, speed can be controlled by changing the electromagnetic torque through current control to provide smooth acceleration as well as efficient system performance. The VSI-based driving mode provides a high efficiency conversion of DC power into controlled AC power for the PMSM. Furthermore, the integration of the DAB converter ensures stable dc-link voltage. The inverter also enables precise control of motor speed and torque which makes this system suitable for use in high-performance applications of electric vehicle propulsion.

B. Proposed Model Predictive Control Scheme for PMSM Speed Regulation

In drive mode operation, the Permanent Magnet Synchronous Motor (PMSM) operates at a fixed speed that is determined by a model predictive controller (MPC), shown in FIGURE 7. The combination of an Artificial Neural Network (ANN) for a Speed Loop and an FCS-based Model Predictive Controller (FCS-MPC) utilizing the FCS-MPC technique, determines the switching conditions of the voltage source inverter. The ANN controller Layer utilizes the speed error as the input and generates the Reference Currents $i_{q,ref}$. Since the d-axis current reference $i_{d,ref} = 0$ is then selected in order to provide decoupled torque control and Minimized Losses; thus eliminating the necessity to find accurate values of the q-axis and d-axis current components of the current. The three-phase stator currents i_{abc} are transformed from Stationary Coordinates to the Rotating dq coordinates using the Electrical Angle of the Rotor θ. These current components in dq-coordinates are then used by the MPC-block to calculate the future development of the current behavior and to choose the best possible switching state of the voltage-source inverter.

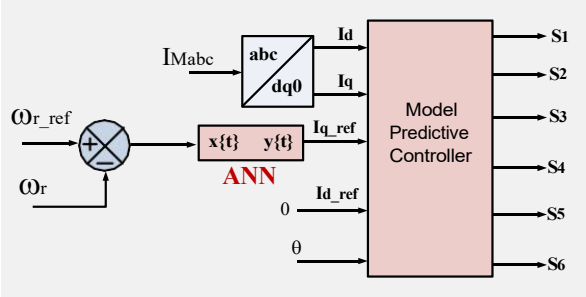

Fig.7 ANN-Assisted Model Predictive Control Scheme for PMSM Speed Regulation

Acquiring the speed error begins with

$$e_\omega(k) = \omega_{r,ref}(k) - \omega_r(k) \quad (57)$$

$\omega_{r,ref}$ represents the reference rotor speed, whereas ω_r stands for the measured rotor speed. The current reference that produces torque is created by the ANN controller using this error, which is expressed as

$$i_{q,ref}(k) = ANN(e_\omega(k), \Delta e_\omega(k)) \quad (58)$$

$\Delta e_\omega(k)$ represents the variance in speed error. For surface-mounted PMSMs, the reference d-axis current is chosen as zero since that is how most of the time they are operated.

$$i_{d,ref}(k) = 0 \quad (59)$$

Using the Clarke-Park transformation, the measured three-phase currents are transformed into the rotating reference coordinate system. Under the synchronous dq reference frame, the, the PMSM stator voltage expressions are given by

$$v_d = Ri_d + L\frac{di_d}{dt} - \omega_e L i_q \quad (60)$$

$$v_q = Ri_q + L\frac{di_q}{dt} - \omega_e L i_d + \omega_e \psi_f \quad (61)$$

where R is the stator resistance, L is the stator inductance, ω_e is the electrical rotational speed, and ψ_f is the permanent-magnet magnetic link. In this predictive control algorithm, the system model was approximated to discrete values using the first order Forward Euler method with a sample interval of Ts. As such, the d-q axis current predictions for the next sampled instant can be expressed as

$$i_d(k+1) = (1 - \frac{RT_s}{L}) i_d(k) + T_s i_q(k) + \frac{T_s}{L} v_d(k) \quad (62)$$

$$i_q(k+1) = (1 - \frac{RT_s}{L}) i_q(k) + T_s i_d(k) - \psi_f T_s + \frac{T_s}{L} v_q(k) \quad (63)$$

The MPC algorithm evaluates all possible switching states of the two-level three-phase inverter. Since the inverter has eight

possible switching combinations, the candidate switching set is defined as

$$S = \{000, 001, 010, 011, 100, 101, 110, 111\}$$

For each switching state, the inverter phase voltages are calculated as

$$V_{inva} = \frac{V_{dc}}{3}(2S_a - S_b - S_c) \quad (64)$$

$$V_{invb} = \frac{V_{dc}}{3}(2S_b - S_a - S_c) \quad (65)$$

$$V_{invc} = \frac{V_{dc}}{3}(2S_c - S_a - S_b) \quad (66)$$

The three inverter legs' switching states are denoted by S_a, S_b, and S_c, and V_{dc} represents the DC-link voltage. By using the rotor position angle θ, these voltages are then converted into the synchronous reference frame as

$$v_q = \frac{2}{3}[V_{inva}\cos\theta + V_{invb}\cos(\theta - \frac{2\pi}{3}) + V_{invc}\cos(\theta + \frac{2\pi}{3})] \quad (67)$$

$$v_d = \frac{2}{3}[V_{inva}\sin\theta + V_{invb}\sin(\theta - \frac{2\pi}{3}) + V_{invc}\sin(\theta + \frac{2\pi}{3})] \quad (68)$$

For every switching state, the value of the future currents $i_d(k+1)$ and $i_q(k+1)$ are computed using these expected voltages. The tracking error between the anticipated currents and their reference values is then quantified using a quadratic cost function:

$$J_i = (i_{d,ref} - i_d(k+1))^2 + (i_{q,ref} - i_q(k+1))^2 \quad (69)$$

The optimal switching state is selected as the one that minimizes the cost function, namely

$$S_{opt} = arg\min J_i \quad (70)$$

Once the optimal switching vector has been determined, the controller applies the appropriate gate pulse pattern to the inverter switches S1-S6. The switching table on the inverter was implemented as part of the MATLAB function so that it could map the desired condition (either speed or position) directly to the gating sequence of the inverter which eliminated the need to implement another PWM modulator. Therefore, the controller can generate the best possible switching pulses for the inverter at each sample time. A significant advantage of employing a Method of Artificial Neural Networks (ANN) Assisting a Model Predictive Controller (MPC), is that this will combine the quick dynamic response of predictive controllers, with the ANN's non-linear approximation capabilities. The ANN provides an adaptive reference current command for speed regulation purposes, whereas the MPC selects the optimum inverter switch configuration from all possible configurations available to accurately track the desired current based upon a discrete representation of the motor model. The result of this methodology is improved speed response, lower steady-state errors, and enhanced overall PMSM drive performance across various operating regimes.

$$T_e = \frac{3}{2}p\psi_f i_q \quad (71)$$

in the event when id=0 and p is the quantity of pole pairs. This proves that the q-axis current directly controls the motor torque, which validates using the ANN-generated $i_{q,ref}$ as the output for speed control. Overall, the proposed model predictive control scheme enables efficient and accurate PMSM speed regulation in driving mode by combining ANN-based reference generation with a finite control set predictive current controller. The method is particularly suitable for EV applications due to its fast response, simple switching-state evaluation, and strong capability to handle the nonlinear dynamics of the PMSM drive system.

VI. ARTIFICIAL NEURAL NETWORK (ANN) CONTROLLER DESIGN

A multilayer feed-forward artificial neural network (ANN) will be used for the control of the power converter on both sides of the system. The use of an ANN instead of traditional PI controllers should allow it to better respond to the non-linear characteristics and uncertainty inherent in power electronics. An ANN serves as a non-linear function approximator mapping the desired inputs (voltage error, current error etc.) to the correct outputs. By doing so, the overall dynamic response improves; the steady state error is minimized; and the overall system stability is increased regardless of variations in operation.

A. ANN Structure

The three primary layers that make up the ANN are:

- Input layer
- Two hidden layers
- Output layer

The input layer receives system error signals, while the hidden layers process the nonlinear relationships between inputs and outputs using activation functions. The output layer generates the control signal required for converter operation.

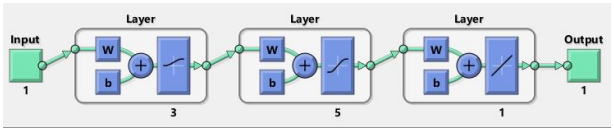

Fig 11: Structure of Neural Network

B. Mathematical Formulation

1. Input Signals

The ANN receives the system error and its rate of change as inputs:

$$x(k) = [e(k), \dot{e}(k)]$$

where:

- $e(k) = r(k) - y(k)$ is the error between reference and actual value
- $\dot{e}(k)$ represents the rate of change of error

2. Neuron Model

Each neuron computes a weighted sum of inputs:

$$v_j = \sum_{i=1}^{n} w_{ji}x_i + b_j$$

where:

- w_{ji} = synaptic weight

- b_j = bias term

3. Activation Functions

The ANN employs nonlinear activation functions to capture system dynamics:

- **Sigmoid function (logsig):**

$$f(v) = \frac{1}{1+e^{-v}}$$

- Hyperbolic tangent function (tansig):

$$f(v) = \tan h(v)$$

- Linear function (output layer):

$$f(v) = v$$

4. Forward Propagation

The ANN output is obtained through layer-by-layer computation:

First hidden layer:

$$h_1 = f_1(W_1 x + b_1)$$

Second hidden layer:

$$h_2 = f_2(W_2 h_1 + b_2)$$

Output layer:

$$u(k) = W_3 h_2 + b_3$$

where $u(k)$ represents the control signal.

C. Training Algorithm

The ANN is trained using supervised learning to minimize the error between the desired output and the network output. The performance index is defined as:

$$E = \frac{1}{2}\sum_{k=1}^{N} (d(k) - y(k))^2$$

where:

- $d(k)$) is the desired output
- $y(k)$ is the ANN output

The weights are updated iteratively to minimize this error using an optimization-based learning algorithm, enabling fast convergence and accurate prediction.

D. ANN Control Law

The ANN generates the control signal directly based on system error:

$$u(k) = ANN(e(k), \dot{e}(k))$$

This control signal is used for:

- Generating PWM duty cycles
- Regulating converter switching
- Controlling voltage and current

E. Application in Proposed EV System

1. Grid-Side Converter (Totem-Pole PFC)

The ANN regulates DC-link voltage and input current:

$$i_{ref} = ANN(V_{dc\_error}, \dot{V}_{dc\_error})$$

2. EV-Side Converter (DAB Converter)

The ANN controls bidirectional power flow:

$$P_{ref} = ANN(e_{battery}, \dot{e}_{battery})$$

VII. SIMULATION RESULTS AND DISCUSSION

A. Bidirectional EV Charging Operation between Grid and Vehicle (G2V and V2G Modes)

The bidirectional EV charging system was modeled and analyzed through MATLAB to assess its performance during grid-to-vehicle (G2V) and vehicle-to-grid (V2G) operational conditions as shown in figure 8. The proposed system consists of an interleaved totem-pole AC/DC converter together with a Dual Active Bridge (DAB) dc–dc converter that are supported by advanced control strategies for stabilized and efficient operation. In the case of G2V, power flows from the utility grid to the EV battery pack. During this stage, the front-end stage interleaved totem-pole topology converter performs AC–DC conversion with inherent power factor correction ensuring the input current accurately tracks the waveform of the input voltage. Results indicate that the input current is practically sinusoidal and has a power factor of approximately 0.98 therefore indicates high-quality interaction between the grid and the EV. Additionally, use of an interleaved configuration effectively reduces output ripple current and increases efficiency. The output dc link voltage is well regulated at reference value with minimal over shoot and fast settling time. On the battery side, the DAB converter functions using a constant current–constant voltage (CC–CV) control strategy which ensures smooth charging while controlling the amount of current delivered and gradually raising the battery voltage. When operating in V2G, power flows back into the grid from the EV battery. The DAB enables reverse power delivery to the utility grid while sustaining a stabilized output DC-link voltage; the front-stage converter operates as a grid connected inverter. Furthermore, the current injected into the grid remains sinusoidal while remaining synchronized with the grid voltage ensuring low harmonic distortion and robust power delivery. Transitions between G2V & V2G modes occur smoothly without significant transient response demonstrating the proposed systems robustness

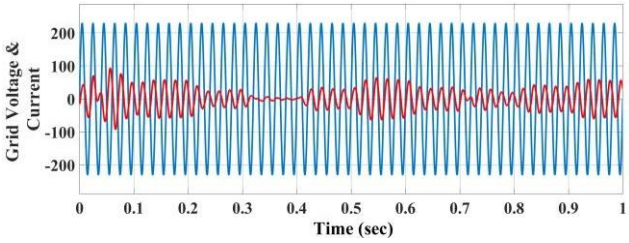

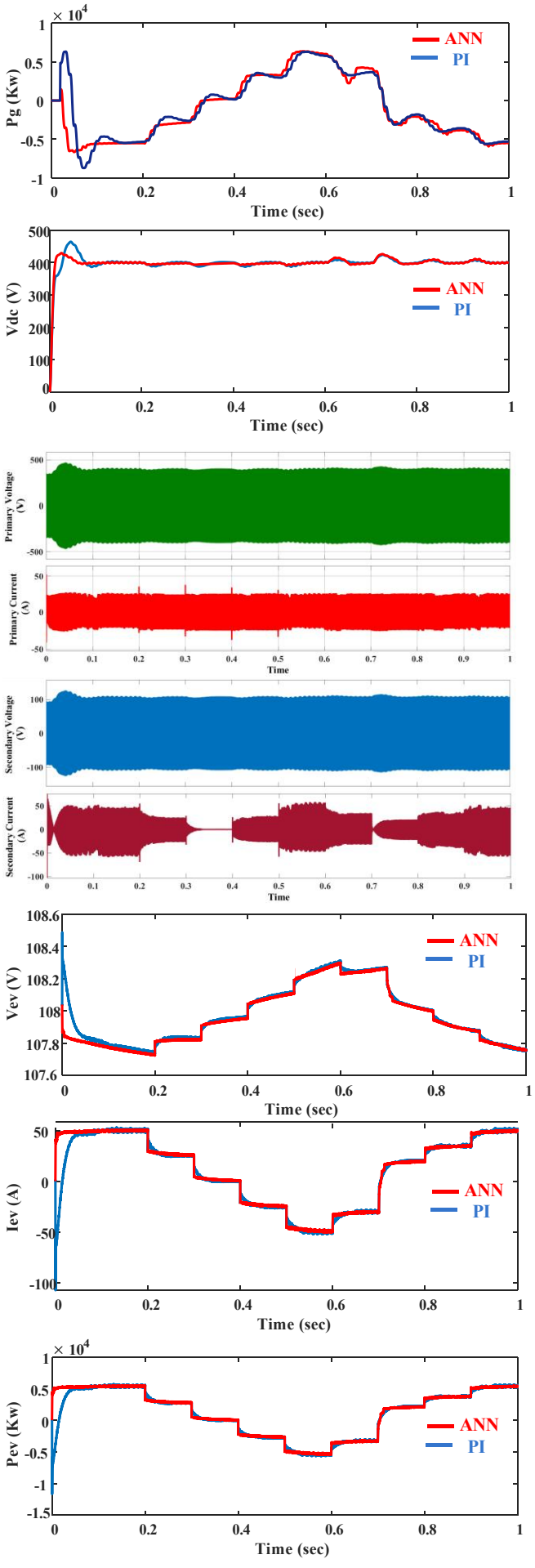

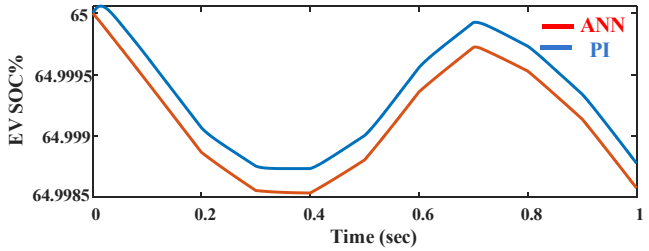

Fig.8 Simulation results of Bidirectional EV Charging Operation between Grid and Vehicle (G2V and V2G Modes)

B. Motor Drive and Regenerative Braking Operation

The efficiency of the proposed electric vehicle (EV) motor drive system can be evaluated through Simulations utilizing MATLAB/Simulink. The dual-mode operation of the motor (motoring and regenerative braking) shown in Fig. 9, is simulated. A battery is coupled to a Dual Active Bridge (DAB)-based converter that is in turn connected to a a Voltage Source Inverter (VSI) that supplies three-phase AC power to a Permanent Magnet Synchronous Motor (PMSM). The focus will be placed toward power flow, torque-speed characteristics and stability under bidirectional operation. During motoring mode, the EV battery packs functions serving the primary energy source, transferring power to the PMSM through the DAB converter and VSI. The DAB Converter regulates the DC-link voltage while the VSI converts the DC power into a three phase AC wave form that powers the motor. Simulation data indicates that the motor could successfully operate at positive speeds and positive torques (normal driving conditions), where stator currents are balanced and very close to sinusoidal indicating good current regulation by the VSI. Additionally, the results show the DC link voltage is constant with minimal ripple under normal operation of the system. Once entering into regenerative braking mode, the operating conditions of the PMSM undergo such a drastic change that instead of consuming electrical energy and converting it into mechanical energy, the PMSM now consumes mechanical energy and produces electrical energy. Since the motor is generating electrical energy, the direction of current changes and therefore power starts flowing back from the PMSM to the DC link. At this stage, the DAB Converter transitions into its reverse configuration returning the captured electrical energy to the battery for recharging purposes. Results from these simulations clearly depict a smooth reversal of current directions without large variations in voltages when changing from motoring to regenerative braking modes. Results from the simulations also show that the proposed system operated smoothly throughout these transitions with little-to-no large amplitude oscillations/overshoot. Through employment of Artificial Neural Network (ANN) and Model Predictive Control (MPC) techniques, much faster transient responses occur with improved speed tracking accuracy and greater system stability. In conclusion, the proposed system efficiently utilizes all available energy, reliably transfers bi-directionally and effectively performs regenerative braking operations providing it to be a prime candidate for future generation EV systems.

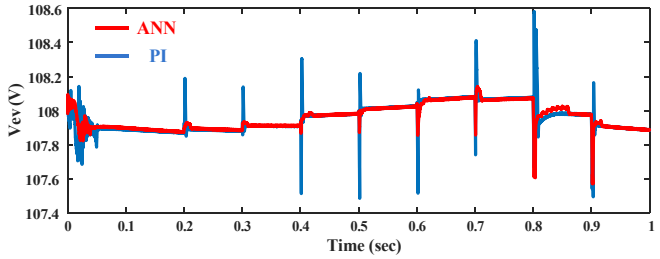

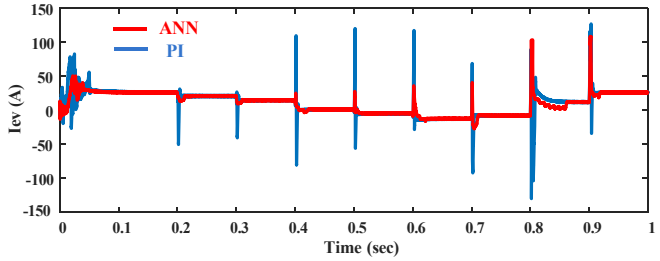

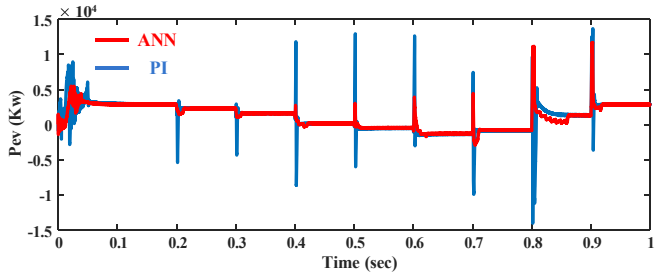

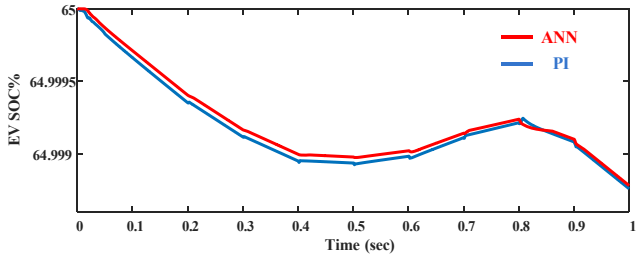

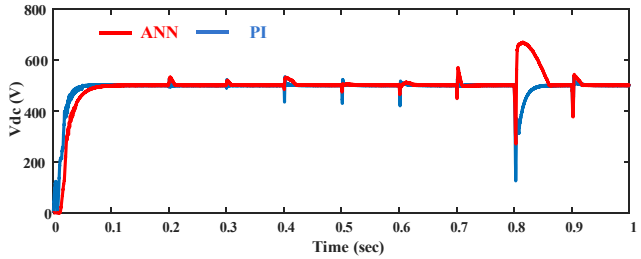

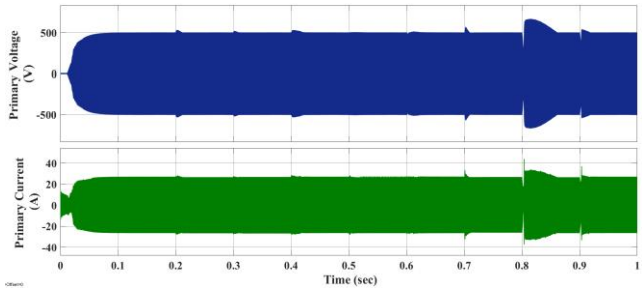

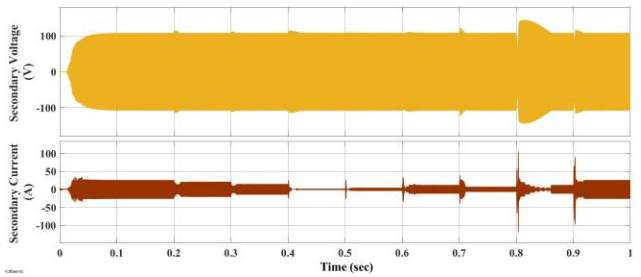

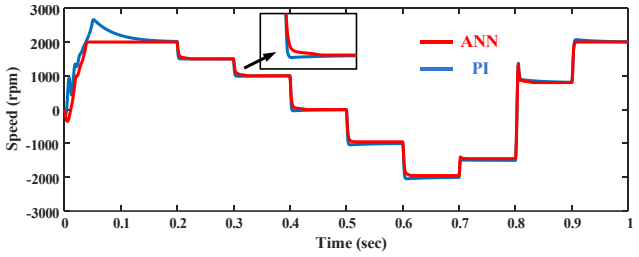

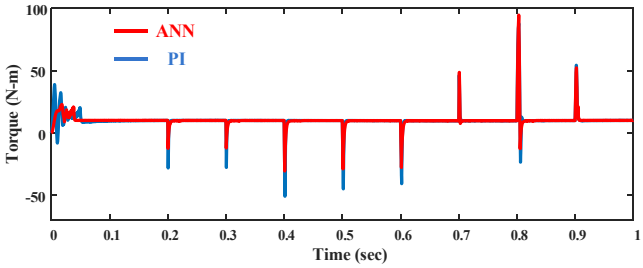

Fig.9 Simulation results of Motor Drive and Regenerative Braking Operation

Table 1. Comparison details of ANN and PI controller for Vdc.

Parameters	ANN	PI
Rise Time (s)	0.0076	0.0150
Settling Time (s)	0.0524	0.1045
Peak Time (s)	0.0254	0.0456
Overshoot Time(ms)	7.7691	15.9340
Peak (V)	429.4476	464.3775

Table 2. Comparison details of ANN and PI controller for Pg.

Parameters	ANN	PI
Rise Time (s)	0.0104	0.0090
Settling Time (s)	0.0927	0.1680
Peak Time (s)	0.0500	0.0724
Overshoot Time(ms)	20.8427	63.1274
Peak (Kw)	6.6548	8.7169

Table 3. Comparison details of ANN and PI controller for Pev.

Parameters	ANN	PI
Rise Time (s)	0.0041	0.0259
Settling Time (s)	0.3949	0.5042
Peak Time (ms)	0.3032	26
Overshoot Time(ms)	1.7854	4.8947
Peak (Kw)	5.4863	11.635

Table 4 Performance Comparison of Power Converter Topologies for EV Charging Applications

References	Main structure	Power (Kw)	Freq. (Khz)	Peak Efficiceny
[8]	IPOS bridgeless PFC + dual buck–boost converters + rectifier only	>1	50	90
[9]	Bridgeless SEPIC PFC rectifier + bidirectional switch + coupled inductors + rectifier only	>1	50	91.8
[13]	Full-bridge converter + phase-modulated resonant transition converter + dual transformers + rectifier only	1	100	85
[15]	Modified SEPIC converter + capacitor–diode voltage multiplier + bidirectional power stage	>1	66	94
[19]	Impedance network + switching network (push–pull) + isolated transformer + voltage multiplier rectifier only	>1	16	91
[24]	DD coupling coils (Tx + Rx) + passive electromagnetic sensing coils (C-shape + patch coil)	3	85	90
This paper	Bidirectional Three-phase PFC + Bidirectional DAB converter + power quality + system stability improvement	6.6	65-100	95

VIII. CONCLUSION

This paper developed an on-board charger and motor drive for electric vehicles (EVs), consisting of both a n interleaved totem-pole AC/DC converter together with a Dual Active Bridge (DAB) DC–DC converter. The proposed integrated design is capable of providing the functions of charging and driving as part of one system, thereby minimizing hardware, reducing complexity and overall system size, increasing system efficiency and power density. The interleaved totem-pole converter efficiently converts from AC to DC at the input side with built-in Power Factor Correction (PFC), minimized conduction loss and reduced output AC ripple. The DAB also provides galvanic isolation and allows for bi-directional power transfer among the grid, battery, and motor grid, battery and motor. By coordinating the two converters for simultaneous or sequential use, it allows for smooth transitions between charging/discharging and driving modes. To improve the performance of this hybrid system, Artificial Neural Network (AN5N) based controls were applied. The ANN controller has improved time-domain response, voltage stability and fault tolerance of the system across an extensive range of operating conditions. In addition, Model Predictive Control strategy (MPC) was used to control the speed of the Permanent Magnet Synchronous Machine (PMSM) during driving mode. The MPC enabled precise tracking of desired speeds and faster transient responses than conventional controllers. The obtained simulation results generated by MATLAB/Simulink confirm that the developed system can operate at high efficiencies and low THD levels with stable behavior over a wide number of operating conditions.

REFERENCES

[1] Jia, C.; He, H.; Zhou, J.; Li, J.; Wei, Z.; Li, K. Learning-based model predictive energy management for fuel cell hybrid electric bus with health-aware control. Appl. Energy 2024, 355, 122228.

[2] U.S. Environmental Protection Agency. Sources of Greenhouse Gas Emissions. 2025. Available online: https://www.epa.gov/ghgemissions/sources-greenhouse-gas emissions (accessed on 5 March 2025).

[3] International Energy Agency. Transport Sector CO2 Emissions by Mode in the Sustainable Development Scenario, 2000–2030. 2019. Available online: https://www.iea.org/data-and-statistics/charts/transport-sector-co2-emissions-by-mode-in-the-sustainabledevelopment- scenario-2000-2030 (accessed on 27 May 2019).

[4] Metwly MMY, Abdel-Majeed MS, Abdel-Khalik AS (2020) A review of integrated on-board EV battery chargers: advanced topologies, recent developments and optimal selection of FSCW slot/pole combination. IEEE Access 8:85216–85242.

[5] J. C. Salmon, ``Circuit topologies for single-phase voltage-doubler boost rectifiers," *IEEE Trans. Power Electron.*, vol. 8, no. 4, pp. 521_529, Oct. 1993.

[6] H.-S. Youn, J.-S. Park, K.-B. Park, J.-I. Baek, and G.-W. Moon, ``A digital predictive peak current control for power factor correction with low input current distortion," *IEEE Trans. Power Electron.*, vol. 31, no. 1, pp. 900_912, Jan. 2016.

[7] F. C. Lee, Q. Li, Z. Liu, Y. Yang, C. Fei, and M. Mu, ``Application of GaN devices for 1 kW server power supply with integrated magnetics," *CPSS Trans. Power Electron. Appl.*, vol. 1, no. 1, pp. 3_12, Dec. 2016.

[8] Z. Chen, B. Liu, Y. Yang, P. Davari, and H. Wang, ``Bridgeless PFC topology simplification and design for performance benchmarking," *IEEE Trans. Power Electron.*, vol. 36, no. 5, pp. 5398_5414, May 2021.

[9] E. H. Ismail, ``Bridgeless SEPIC rectifier with unity power factor and reduced conduction losses," *IEEE Trans. Ind. Electron.*, vol. 56, no. 4, pp. 1147_1157, Apr. 2009.

[10] B. Zhao, A. Abramovitz, and K. Smedley, ``Family of bridgeless buckboost PFC rectifiers," *IEEE Trans. Power Electron.*, vol. 30, no. 12, pp. 6524_6527, Dec. 2015.

[11] F. Musavi, W. Eberle, and W. G. Dunford, ``A high-performance single phase bridgeless interleaved PFC converter for plug-in hybrid electric vehicle battery chargers," *IEEE Trans. Ind. Appl.*, vol. 47, no. 4, pp. 1833_1843, Jul. 2011.

[12] T. T.Vu and E. Mickus, ``99% ef_ciency 3-level bridgeless totem-pole PFC implementation with low-voltage silicon at low cost," in *Proc. IEEE Appl. Power Electron. Conf. Expo. (APEC)*, Mar. 2019, pp. 2077_2083.

[13] N. Swaminathan and N. Lakshminarasamma, ``The steady-state DC gain loss model, efficiency model, and the design guidelines for high-power, high-gain, low-input voltage DC_DC converter," *IEEE Trans. Ind. Appl.*, vol. 54, no. 2, pp. 1542_1554, Mar. 2018.

[14] Q. Huang, Q. Ma, P. Liu, A. Q. Huang, and M. A. de Rooij, ``99% ef_cient 2.5-kW four-level _ying capacitor multilevel GaN totem-pole PFC," *IEEE J. Emerg. Sel. Topics Power Electron.*, vol. 36, no. 5, pp. 6046_6055, Mar. 2021.

[15] Fardoun, A.A.; Ismail, E.H.; Sabzali, A.J.; Al-Saffar, M.A. Bidirectional converter for high-efficiency fuel cell powertrain. J. Power Sources 2014, 249, 470–482.

[16] Matsuo, H.; Kurokawa, F. New solar cell power supply system using a boost type bidirectinal DC-DC converter. IEEE Trans. Ind. Electron. 1984, IE-31, 51–55.

[17] Zhang, J.; Lai, J.S.; Yu, W. Bidirectional DC-DC converter modeling and unified controller with digital implementation. In Proceedings of the 2008 Twenty-Third Annual IEEE Applied Power Electronics Conference and Exposition, Austin, TX, USA, 24–28 February 2008; pp. 1747–1753.

[18] Jia, C.; He, H.; Zhou, J.; Li, K.; Li, J.; Wei, Z. A performance degradation prediction model for PEMFC based on bi-directional long short-term memory and multi-head self-attention mechanism. Int. J. Hydrogen Energy 2024, 60, 133–146.

[19] Gorji, S.; Ektesabi, M.; Zheng, J. Isolated switched-boost push–pull DC–DC converter for step-up applications. Electron. Lett. 2017, 53, 177–179.

[20] Jia, C.; Zhou, J.; He, H.; Li, J.; Wei, Z.; Li, K. Health-conscious deep reinforcement learning energy management for fuel cell buses integrating environmental and look-ahead road information. Energy 2024, 290, 130146.

[21] Kumar, A.; Bhat, A.; Agarwal, P. Comparative analysis of dual active bridge isolated DC to DC converter with flyback converters for bidirectional energy transfer. In Proceedings of the 2017 Recent Developments in Control, Automation & Power Engineering (RDCAPE), Noida, India, 26–27 October 2017; pp. 382–387.

[22] Li, X.; Bhat, A.K. Analysis and design of high-frequency isolated dual-bridge series resonant DC/DC converter. IEEE Trans. Power Electron. 2009, 25, 850–862.

[23] Liu, Y.C.; Chen, C.; Chen, K.D.; Syu, Y.L.; Dung, N.A. High-frequency and high-efficiency isolated two-stage bidirectional DC–DC converter for residential energy storage systems. IEEE J. Emerg. Sel. Top. Power Electron. 2019, 8, 1994–2006.

[24] Niu, S.; Niu, S.; Zhang, C.; Jian, L. Blind-Zone-Free Metal Object Detection for Wireless EV Chargers Employing DD Coils by Passive Electromagnetic Sensing. IEEE Trans. Ind. Electron. 2023, 70, 965–974.

[25] Niu, S.; Zhao, Q.; Chen, H.; Niu, S.; Jian, L. Noncooperative Metal Object Detection Using Pole-to-Pole EM Distribution Characteristics forWireless EV Charger Employing DD Coils. IEEE Trans. Ind. Electron. 2024, 71, 6335–6344.

[26] Hao, Z.; Zhu, H.; Cheng, Y.; Huang, L. Speed Control of Bearingless Permanent Magnet Synchronous Motor Based on Flux Strengthening and Voltage Regulation. IEEE Access 2018, 6, 72392–72401.

[27] Sun, X.; Zhang, Y.; Cai, Y.; Tian, X. Compensated deadbeat predictive current control considering disturbance and VSI nonlinearity for in-wheel PMSMs. IEEE/ASME Trans. Mechatron. 2022, 27, 3536–3547.

[28] Li, T.; Sun, X.; Lei, G.; Yang, Z.; Guo, Y.; Zhu, J. Finite-control-set model predictive control of permanent magnet synchronous motor drive systems—An overview. IEEE/CAA J. Autom. Sinica 2022, 9, 2087–2105.

[29] Faiz, J.; Mohseni-Zonoozi, S.H. A novel technique for estimation and control of stator flux of a salient-pole PMSM in DTC method based on MTPF. IEEE Trans. Ind. Electron. 2003, 50, 262–271.

[30] Sun, X.; Hu, C.; Lei, G.; Yang, Z.; Guo, Y.; Zhu, J. Speed sensorless control of SPMSM drives for EVs with a binary search algorithm-based phase-locked loop. IEEE Trans. Veh. Technol. 2020, 69, 4968–4978.

[31] Junejo, A.K.; Xu,W.; Mu, C.; Ismail, M.M.; Liu, Y. Adaptive Speed Control of PMSM Drive System Based a New Sliding-Mode Reaching Law. IEEE Trans. Power Electron. 2020, 35, 12110–12121.

[32] Sun, X.; Tang, X.; Tian, X.; Lei, G.; Guo, Y.; Zhu, J. Sensorless control with fault-tolerant ability for switched reluctance motors. IEEE Trans. Energy Convers. 2022, 37, 1272–1281.

[33] Chai, S.; Wang, L.; Rogers, E. A cascade MPC control structure for a PMSM with speed ripple minimization. IEEE Trans. Ind. Electron. 2013, 60, 2978–2987.

[34] Sun, X.; Cao, J.; Lei, G.; Guo, Y.; Zhu, J. A robust deadbeat predictive controller with delay compensation based on composite sliding mode observer for PMSMs. IEEE Trans. Power Electron. 2021, 36, 10742–10752.

[35] Li, Y.; Ruan, X.;Wang, Y.; Zhang, C. Hysteresis Voltage Prediction Control for Multilevel Converter in the Series-Form Switch- Linear Hybrid Envelope Tracking Power Supply. IEEE Trans. Power Electron. 2020, 35, 13663–13672.

[36] Huang, S.-D.; Chen, L.; Cao, G.-Z.; Wu, C.; Xu, J.; He, Z. Predictive Position Control of Planar Motors Using Trajectory Gradient Soft Constraint with Attenuation Coefficients in the Weighting Matrix. IEEE Trans. Ind. Electron. **2021**, 68, 821–837.

[37] Sun, X.; Shi, Z.; Lei, G.; Guo, Y.; Zhu, J. Multi-objective design optimization of an IPMSM based on multilevel strategy. IEEE Trans. Ind. Electron. **2021**, 68, 139–148.

[38] G. McClone, A. Ghosh, A. Khurram, B. Washom, and J. Kleissl, "Hybrid machine learning forecasting for online MPC of work place electric vehicle charging," IEEE Trans. Smart Grid, vol. 15, no. 2, pp. 1891–1901, Mar. 2024.

[39] B. Wang, P. Dehghanian, and D. Zhao, "Coordinated planning of electric vehicle charging infrastructure and renewables in power grids," IEEE Open Access J. Power Energy, vol. 10, pp. 233–244, 2023.

[40] B. Adineh, M. R. Habibi, A. N. Akpolat, and F. Blaabjerg, "Sensorless voltage estimation for total harmonic distortion calculation using artificial neural networks in microgrids," IEEE Trans. Circuits Syst. II, Exp. Briefs, vol. 68, no. 7, pp. 2583–2587, Jul. 2021.

[41] Z. J. Lee et al., "Adaptive charging networks: A framework for smart electric vehicle charging," IEEE Trans. Smart Grid, vol. 12, no. 5, pp. 4339–4350, Sep. 2021.

[42] H. Tu, H. Feng, S. Srdic, and S. Lukic, "Extreme fast charging of electric vehicles: A technology overview," IEEE Trans. Transport. Electrific., vol. 5, no. 4, pp. 861–878, Dec. 2019.

[43] Manthiram, A. (2020). A reflection on lithium-ion battery cathode chemistry. *Nature communications*, *11*(1), 1550.

[44] Pattipati, Bharath, B. Balasingam, Gopi Vinod Avvari, Krishna R. Pattipati, and Y. Bar-Shalom. "Open circuit voltage characterization of lithium-ion batteries." *Journal of Power Sources* 269 (2014): 317-333.